Earth and Planetary Science Letters 498 (2018) 129–139

Contents lists available at ScienceDirect

Earth and Planetary Science Letters

www.elsevier.com/locate/epsl

Diffusion geospeedometry in natural and experimental shear zones

W.O. Nachlas [a,b,*], C. Teyssier [a], D.L. Whitney [a], G. Hirth [c]

[a] *Department of Earth Sciences, University of Minnesota, Minneapolis, MN 55455, United States of America*
[b] *Department of Earth Sciences, Syracuse University, Syracuse, NY 13244, United States of America* [1]
[c] *Department of Earth, Environmental, and Planetary Sciences, Brown University, Providence, RI 02912, United States of America*

ARTICLE INFO

Article history:
Received 12 June 2018
Accepted 18 June 2018
Available online 5 July 2018
Editor: A. Yin

Keywords:
geospeedometry
deformation
trace element diffusion
ductile shear zones
extensional tectonics
rutilated quartz

ABSTRACT

A new method for determining the timescales of ductile deformation utilizes diffusion profiles around oriented mineral inclusions. This geospeedometer was tested with rutile needle inclusions in mylonitized quartz grains because they are sensitive to the kinematics of deformation and behave as diffusion couples that can be either a source or sink for Ti diffusion in the host quartz. The method was applied to experimental samples, in which the time–temperature conditions are known, and to natural samples, in which the time–temperature conditions are determined using independent geochronometers and geothermometers. In our experimental quartzite, rutile needles become included in quartz during isostatic annealing, rotate into the elongation direction of shearing during imposed deformation, and act as a source of Ti for the surrounding undersaturated quartz. Diffusion modeling of Ti enrichment halos yields appropriate trends in experiment duration. In a natural quartzite mylonite from the extensional detachment zone of the Pioneer Core Complex (Idaho, USA), quartz grains are densely and pervasively rutilated. Titanium depletion halos in quartz around lineated and boudinaged rutile needles indicate that rutile exsolved during deformation. By estimating temperature from quartz microstructures and Ti-in-quartz thermometry, diffusion modeling results suggest that ductile deformation in the shear zone lasted 5–10 Myr, consistent with geologic and thermochronologic data defining exhumation of the complex. Considering structural offsets across the detachment, extrapolating our lab-derived diffusivities to the conditions of natural samples equates to strain rates of $\sim 1 \times 10^{-12}$ s^{-1}. Tests of geospeedometry in both naturally and experimentally deformed rutilated quartz samples indicate that this method can provide reliable information on shear zone longevity and strain rate directly from the phase controlling the rheological behavior of deformation.

1. Introduction

The duration and rates of ductile deformation in shear zones are first-order parameters in the geodynamics of orogens. Strategies to determine the longevity of shear zones have focused primarily on linking isotope ages with structural features; for example, dating dikes that cross-cut or are transposed by ductile fabrics (e.g. Phillips et al., 2004; Sassier et al., 2009), dating minerals that reset during deformation and recrystallization (e.g. Dunlap et al., 1991; Freeman et al., 1998; Williams and Jercinovic, 2002; Mulch and Cosca, 2004; Schneider et al., 2013), or dating crystallization in structural sites that can be correlated with deformation kinematics (e.g. Müller et al., 2000; Sherlock et al., 2003). These approaches use isotope ages from spatially-correlated samples and estimates of structural offset from field observations to evaluate the timescales over which shear zones were active. Diffusion geospeedometry introduces a complementary method, capable of determining shear zone longevity directly from the mineral controlling the deformation.

With continued advances in experimental determination of diffusion kinetics for many mineral systems (Zhang and Cherniak, 2010, and references therein), there are new opportunities to retrieve information on the timescales of high-temperature geologic processes by modeling incomplete diffusion profiles trapped in minerals. This approach has driven applications of geospeedometry, a method that uses diffusion kinetics as a clock to extract rates and thermal histories of geologic processes (Watson and Baxter, 2007; Chakraborty, 2008). Because it is not dependent on the half-life of an isotopic system, geospeedometry can resolve very short timescales, even in ancient rocks in which such short events

---

* Corresponding author.
E-mail address: wnachlas@syr.edu (W.O. Nachlas).
[1] Present address.

https://doi.org/10.1016/j.epsl.2018.06.025

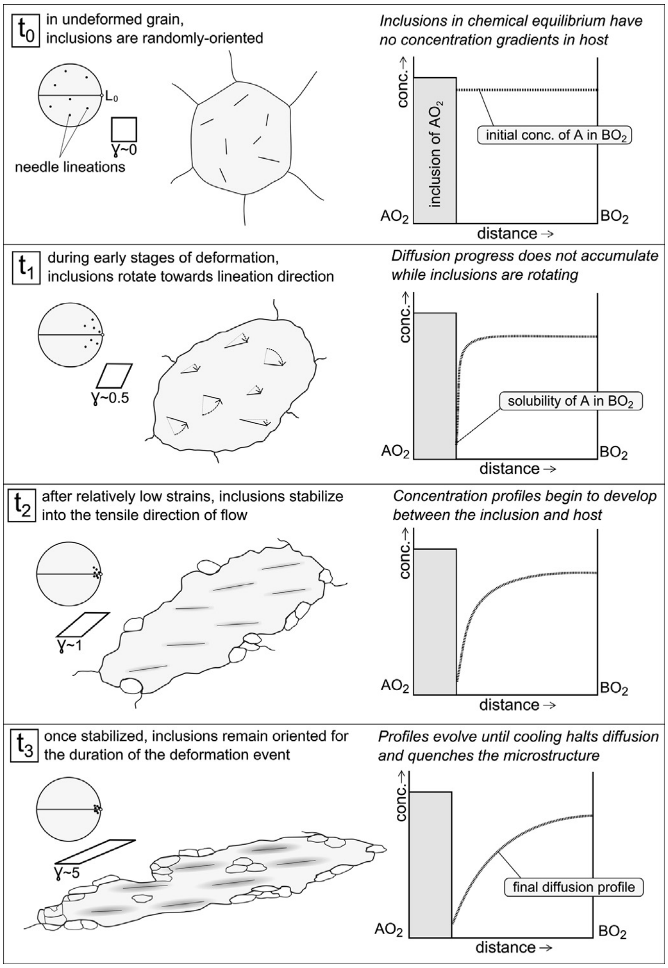

Fig. 1. Shear zone geospeedometry uses incomplete diffusion halos around structurally-oriented mineral inclusions to link diffusive timescales with deformation kinematics. The assumed starting condition (t_0) is an undeformed host grain with randomly-oriented inclusions (here, with composition AO_2) that are at chemical equilibrium with their host (here, BO_2). During early stages of deformation (t_1), inclusions rotate towards the lineation direction of deformation. With a decrease in solubility, the host phase will begin to diffuse component A towards the inclusion phase, but since inclusions are rotating within the host grain matrix, diffusion progress does not accumulate. High aspect ratio inclusions rotate into a stable orientation after relatively low strains (t_2), and the geospeedometry clock "starts" as a measurable concentration profile begins to develop. Progressive deformation will not re-orient inclusions once they have stabilized into the flow direction (t_3), so diffusion profiles record the amount of time that the needles remained in the lineation direction before cooling quenches the microstructure and halts diffusion progress. Analysis of the mid-concentration distance corresponds to the duration of diffusion within that current orientation and thus provides a minimum estimate of deformation timescales.

cannot be resolved by radiometric methods (e.g. Olker et al., 2003; Camacho et al., 2009).

The premise of shear zone geospeedometry is to link diffusion progress with structural kinematics to provide information on the timescales of deformation events (Fig. 1). During ductile shearing, high aspect ratio mineral inclusions rotate passively toward the long axis of the finite strain ellipse, or lineation direction, and develop a strong shape fabric after relatively small strains (e.g. Mitra, 1976). Our geospeedometry analysis uses diffusion profiles that are symmetrical about the lineated inclusions, thereby providing a minimum estimate of deformation duration (Fig. 1). This method follows the assumption that deformation coincided with a thermal event that governed the diffusion progress, as would be expected given the strong temperature dependence on crystal plasticity.

We test this concept using rutilated quartz mylonites because rutile needle inclusions simultaneously behave as both passive markers of ductile flow and natural quartz-rutile diffusion couples. Quartz is perhaps the most important load-bearing mineral in the continental crust, and because it is a major modal component of many different rock types, its deformation behavior strongly influences the rheology of continental shear zones (e.g., Kohlstedt et al., 1995). In addition to its rheological significance, quartz trace element contents can provide robust thermometry, barometry, and geospeedometry information on the conditions and timescales of growth and recrystallization. With advances in understanding Ti solubility (Wark and Watson, 2006; Thomas et al., 2010) and diffusivity in quartz (Cherniak et al., 2007), both the direction and rates of Ti flux can be predicted and used to interpret geologic events. By combining diffusion analysis with microstructural and trace-element thermometry from the same mineral, deformation geospeedometry provides a new approach to evaluate the strain rates and thermal histories of ductile shear zones.

2. Geospeedometry of rutilated quartz mylonites

The high aspect ratio of rutile needles causes them to rotate and align during plastic strain of quartz (Fig. 2). Lineated and boudinaged rutile needles are commonly observed in deformed quartz-bearing rocks (e.g. Mitra, 1976; Bouchez et al., 1984). Additionally, rutile needles can act as either a Ti sink (Cherniak et al., 2007) or source (Nachlas and Hirth, 2015) during diffusion controlled exchange of the Ti content of the host quartz grains in response to changes in P-T-X conditions. In our natural quartz mylonite samples, cathodoluminescence (CL) maps reveal dark halos around rutile needles (Fig. 3A, B), whereas needles in experimental samples are mantled by bright halos (Fig. 3C, D). Considering the positive correlation between CL and quartz Ti concentrations (e.g. Müller et al., 2003; Leeman et al., 2012), these results suggest that rutile exsolved from quartz in the natural samples and dissolved into quartz in the experimental samples (Fig. 4).

To extract duration information from incomplete diffusion profiles requires a measurement of diffusion progress (e.g. the width of a diffusion profile), an independent estimate of temperature, and diffusion parameters for the system of interest. The experiments of Cherniak et al. (2007) produced an Arrhenius relation for Ti diffusion parallel to the (001) direction in quartz. Their results also indicated modest anisotropy, with diffusivity perpendicular to (001) about 5 times smaller than parallel to (001).

These parameters can be used to construct a diffusion model that best approximates the inferred concentration profiles observed in our samples, from which diffusion time can be calculated. To first-order, diffusion of Ti between rutile needles and the host quartz can be approximated as half-space interdiffusion from an infinite source into a semi-infinite medium. Typically, this would be represented by an error-function solution to fit digital concentration data. However, in the case of our samples in which diffusion occurred during deformation and dynamic recrystallization of the host phase, it is possible that multiple diffusion mechanisms were operative (e.g. through dislocations and grain boundaries), resulting in composite profiles. To avoid errors associated with fitting the distal portions or "tails" of the profiles that may reflect contributions from secondary diffusion mechanisms (Zhang et al., 2007; Clay et al., 2010), we applied the simple and robust square root law for diffusion, $x \approx \sqrt{Dt}$, where x is the mid-concentration distance in m, D is the diffusion coefficient ($m^2\,s^{-1}$) solved at a chosen temperature following Cherniak et al. (2007), and t is time in s.

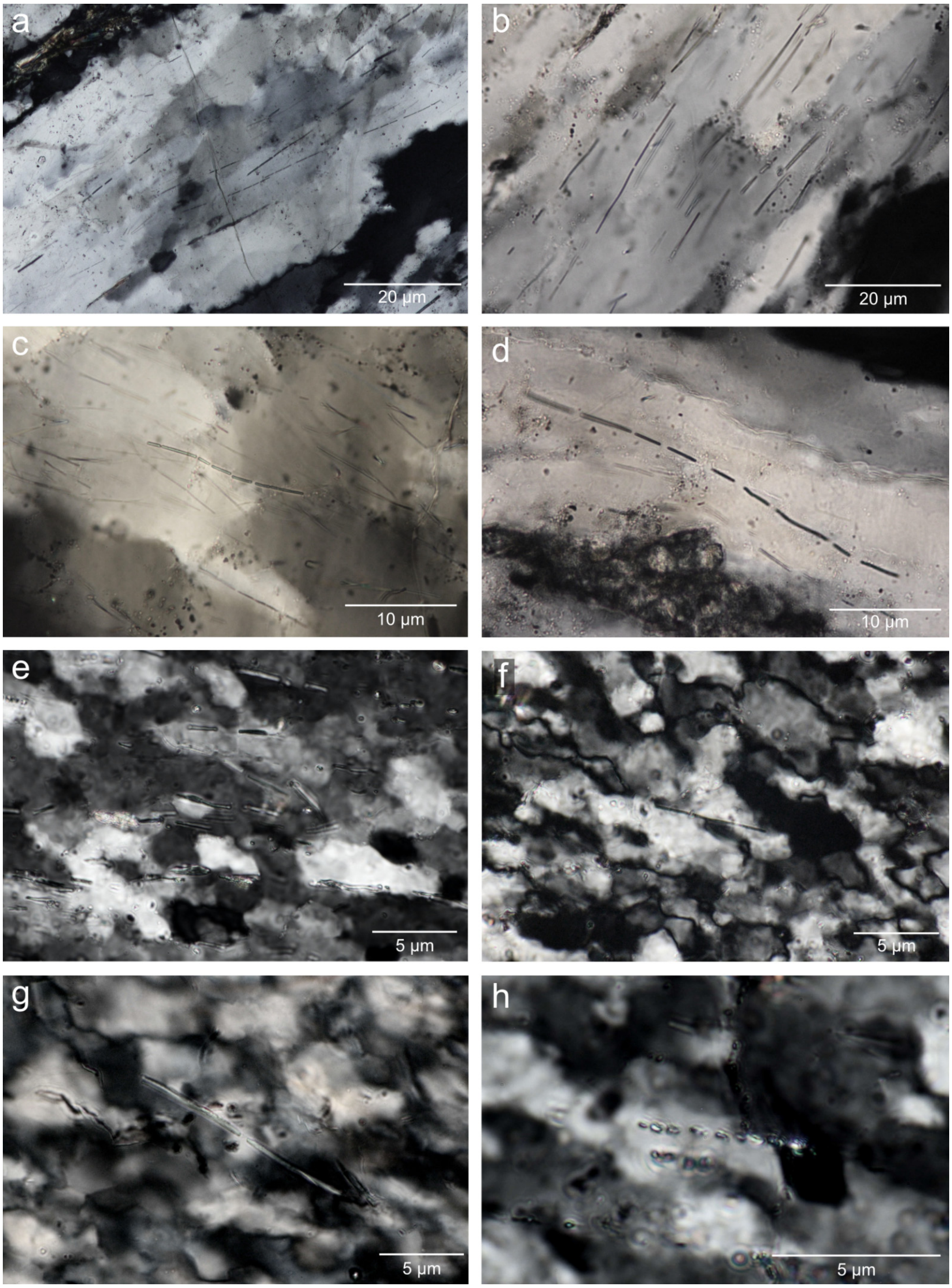

Fig. 2. Cross-polarized light micrographs of rutile needles in quartzite mylonites from the Pioneer Core Complex (A–D) and in synthetic quartz mylonites deformed in experiments (E–H).

3. Analytical methods

In order to resolve short-duration and/or low-temperature geologic events it is necessary to measure very small (c. 1 μm) gradients in concentration. To avoid complications arising from contamination associated with conventional *in situ* techniques, and because of the simplifying assumptions inherent in modeling diffusion at the trace level, we used cathodoluminescence (CL) to semi-quantitatively map Ti contents. CL analysis was conducted with two different electron microscopes and CL detectors: a JEOL-6700F FEG SEM equipped with a Gatan Mono-CL detector (University of Minnesota, College of Science and Engineering Characterization Facility) and a JEOL 5800LV FEG-SEM equipped with a KE Developments CL detector (USGS Denver Microbeam Laboratory). A panchromatic CL spectrum collected from a high-Ti synthetic quartz crystal containing 230 ppm Ti using the UMN-SEM shows a broad peak in the blue range (Nachlas and Hirth, 2015). Hyperspectral CL using the USGS-SEM reveals that the CL signal is dominated by blue luminescence in grain interiors, grain boundaries, and adjacent to acicular rutile inclusions. Based on these observations, taken with past correlations of CL signal and in-situ trace element measurements (e.g. Müller et al., 2003; Leeman et al., 2012), we regard CL intensity as a semi-quantitative proxy for Ti content in quartz. Results of diffusion analysis using CL images collected from both SEMs are statistically indistinguishable and were aggregated for analysis and interpretation.

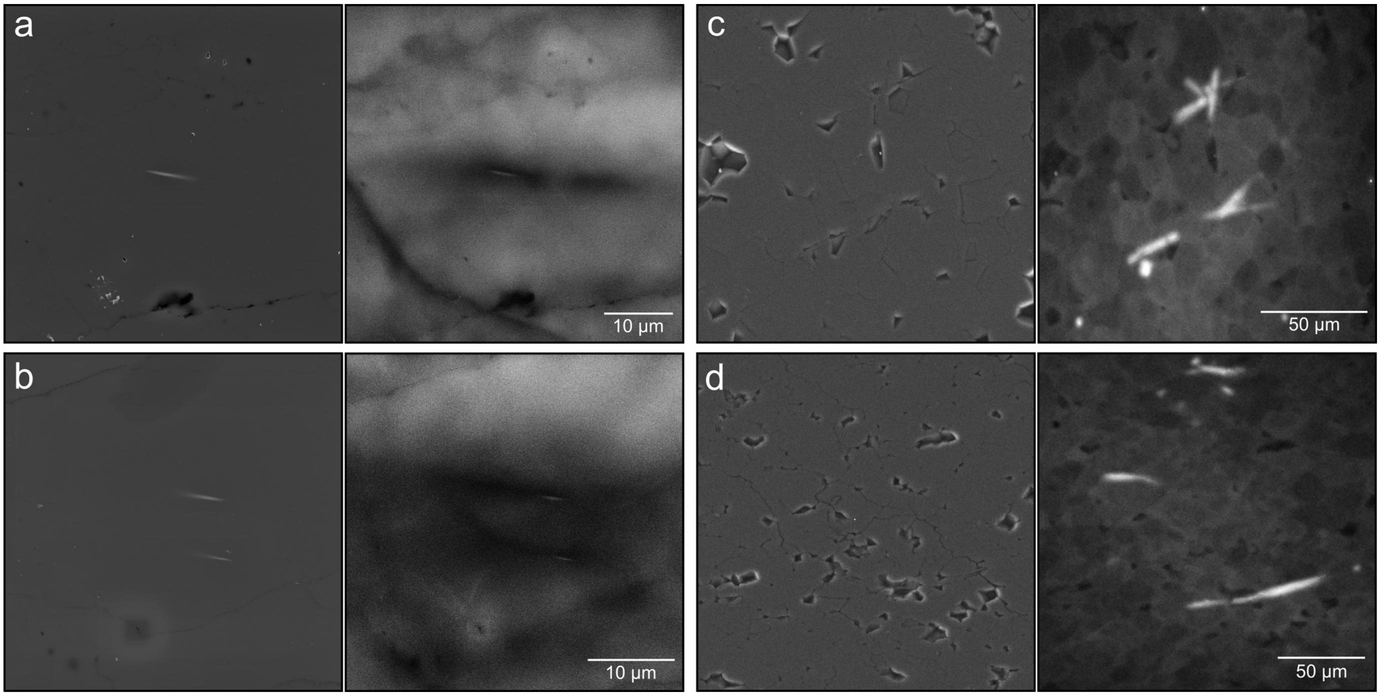

Fig. 3. Secondary electron images (SEI) and cathodoluminescence images (CL) of rutile needle inclusions in natural (A–B) and synthetic (C–D) rutilated quartzites. Dark-CL depletion halos surrounding samples from the Pioneer Core Complex indicate that rutile was exsolving from quartz during deformation, whereas bright-CL resorption halos in experimentally-deformed quartzites indicate that rutile was dissolving into quartz during deformation.

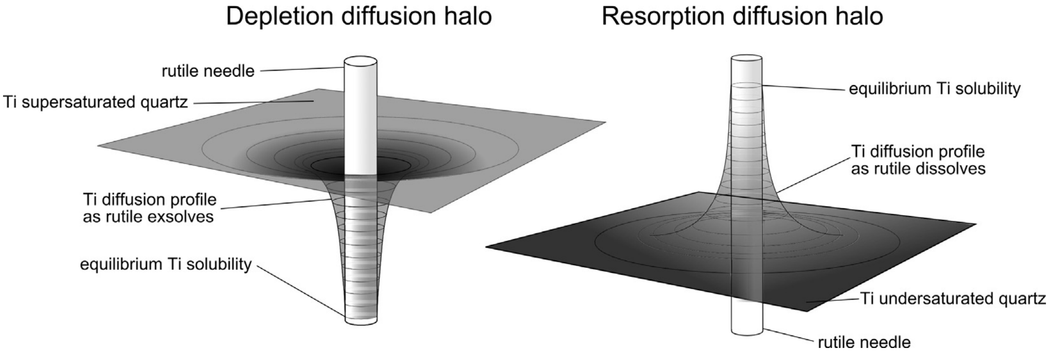

Fig. 4. Illustration of two types of Ti diffusion behavior observed in our rutilated quartz samples. Re-drawn after Cherniak et al. (2007).

The small size and close spacing of rutile needles introduces numerous challenges when attempting to make *in situ* measurements of Ti concentration of rutilated quartz. Electron probe microanalysis (EPMA) offers high spatial resolution, but secondary fluorescence of Ti X-rays from adjacent rutile needles can introduce significant error in measured trace element concentrations even at far distances (>200 µm) from the fluorescing source (e.g. Wark and Watson, 2006). Ion microprobe analysis (SIMS) offers improved sensitivity, and does not suffer from fluorescence, but the larger spot sizes of the ion beam make it difficult to avoid rutile inclusions. We used the Cameca IMS-1280 ion microprobe at Woods Hole Oceanographic Institution to measure Ti contents in thin section samples of rutilated quartz. Results yielded variable Ti measurements within single grains (Fig. S1, Table S1). Analysis craters with 7 µm diameter and 1 µm depth (Nachlas et al., 2014) were apparently too large to avoid rutile needles in the densely rutilated samples. Many of the ion probe measurements yielded high and variable Ti concentrations, which we interpret to reflect contamination from partial ionization of rutile needles. A group of low Ti concentrations are interpreted to reflect uncontaminated measurements of quartz and are used for thermobarometry applications.

4. Application to experimentally deformed quartz

We applied diffusion geospeedometry to a suite of rutilated quartzite samples that were experimentally deformed at constant temperature for increasing intervals of time (Nachlas and Hirth, 2015). In these experiments, rutile needles were dissolving into the host quartz grains during deformation of the sample. Using the known temperature-time conditions we calculate bulk Ti diffusion rates and discuss potential effects of water fugacity and deformation on Ti diffusivities in quartz.

4.1. Experimental methods

Rutilated quartz aggregates were deformed at 1.0 GPa and 900 °C to steady-state flow conditions for three incrementally-longer intervals of time (24, 48, 72 h) (Nachlas and Hirth, 2015). Samples were initially annealed at these P–T conditions for 15 h, and then either held for an additional 24 h “hydrostatic” annealing period or deformed by applying a load at a fixed axial displacement rate of 10^{-6} s^{-1} to achieve a shear strain rate of $\sim 5 \times 10^{-5}$ s^{-1}. This approach resulted in a suite of experiments consisting of an undeformed hydrostatic sample and low-

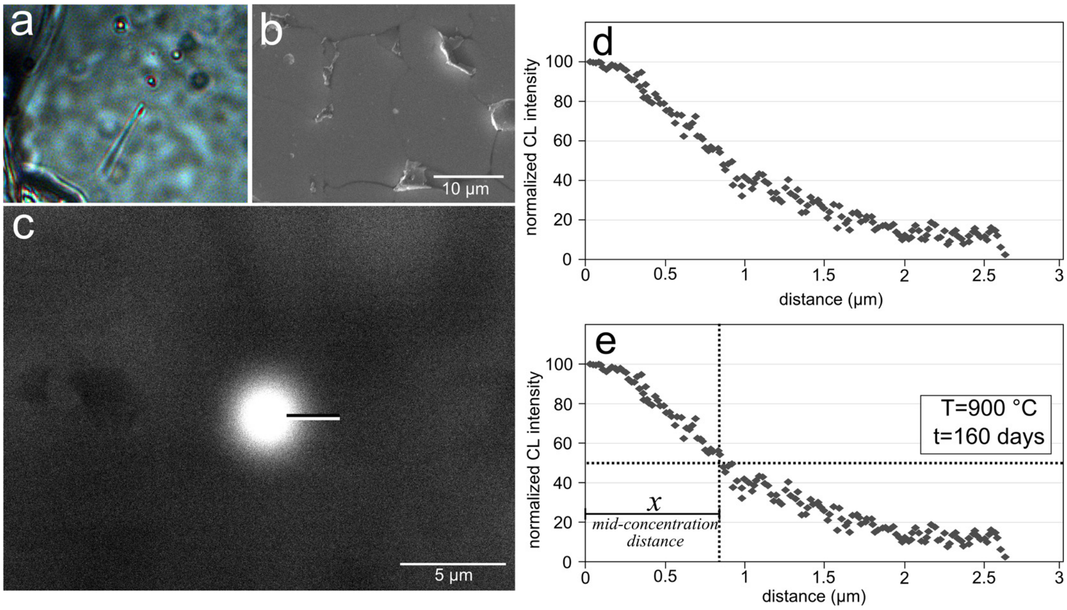

Fig. 5. Technique for modeling Ti diffusion profiles around rutile needles as applied to enrichment halos present in experimental samples. The intersection of a rutile needle with the thin section surface is identified in petrographic microscope (A), detected in a secondary electron image (B), and analyzed with cathodoluminescence (C) to measure the surrounding Ti concentration field. A bright CL halo indicates that Ti diffused from rutile into quartz. The gradient in CL intensity is measured along a linear transect from rutile into the surrounding quartz (C), revealing a composition profile in inferred Ti content that resembles a diffusion profile (D). Profiles are normalized to a concentration percent of 0–100, trimmed from max–min, and the mid-concentration distance is calculated. By assuming a fixed temperature, geospeedometry results indicate durations of c. 100–1000 days for experimentally deformed samples. The overestimation of known experiment durations suggests that the diffusion coefficients applied for our analysis do not fully encompass all diffusion mechanisms operating in our samples.

Table 1
Description of natural and experimental samples and results of geospeedometry analysis.

Sample	Distance below detachment (m)	Ti conc. (ppm)	T from Ti-in-qz (°C)[a]	Water fugacity (GPa)[b]	No. profiles measured	Mean mid-conc. distance (μm)	St.dev mid-conc. distance (μm)	Geospeedometry results	
								t (Myr) (at 500 °C)	Shear strain rate (s^{-1})
WLM-1	100				20	2.25	0.90	6.4	1.1E−12
WLM-2	80				13	2.09	0.66	5.5	1.3E−12
WLM-3	80				20	2.15	0.89	5.8	1.3E−12
WLM-9	30	5.6/0.5	390/275	0.06	41	2.02	0.81	5.1	1.4E−12
WLM-12	10	17.4	460	0.09	25	2.30	0.93	6.7	1.1E−12

Sample	Experiment type	Temperature (°C)	Shear strain rate (s^{-1})	Water fugacity (GPa)[b]	Experiment duration (h)	No. profiles measured	Mean mid-conc. distance (μm)	St.dev. mid-conc. distance (μm)	Geospeedometry results	
									t (days)	$\log D$ ($m^2 s^{-1}$)
W1696	Hydrostatic	900	$5 * 10^5$	1.80	39	140	1.28	0.48	450	−17.0
W1678	Low strain	900	$5 * 10^5$	1.80	39	114	1.16	0.36	350	−17.1
W1680	Mod. strain	900	$5 * 10^5$	1.80	63	23	1.17	0.45	370	−17.4
W1700	High strain	900	$5 * 10^5$	1.80	87	38	2.08	0.51	1100	−16.9

[a] Calculated using the Thomas et al. (2010) calibration and assuming $P = 0.3$ GPa and $a_{TiO_2} = 1$.
[b] Calculated using Pitzer and Sterner (1994) equation of state for pure water.

strain ($\gamma \sim 0.7$), intermediate-strain (∼2), and high-strain (∼3.1) deformed samples.

Rutilated quartz aggregates were synthesized as two layers; one layer was supersaturated in Ti, and the other undersaturated in Ti (with respect to the equilibrium solubility predicted for the P–T conditions of experiments). The quartz layers were produced by doping high-purity silica gel with precise Ti concentrations to produce layers of quartz with Ti concentrations above and below the equilibrium solubility for the experimental conditions (Nachlas and Hirth, 2015). Excess Ti in the supersaturated layer resulted in growth of radiating, randomly-oriented rutile needles in pore spaces of the undersaturated layer, which were included into quartz by migrating grain boundaries during annealing. During deformation, the rutile needles passively rotated into the lineation direction (Fig. 2E–H). As the quartz that incorporated the rutile was Ti undersaturated, Ti dissolved from the needles into the host quartz, forming concentration profiles that were measured with CL and modeled for geospeedometry analysis.

4.2. Geospeedometry applied to experimentally-deformed quartzite

In experimental samples, rutile inclusions emit bright CL halos in the surrounding quartz (Fig. 3C, D). CL halos are radially symmetric around rutile needles oriented sub-perpendicular to the analysis surface and exhibit planar symmetry around needles that are sub-parallel to the analysis surface. Halos become progressively wider and smoother in samples from longer duration experiments (Nachlas and Hirth, 2015).

The CL halos are difficult to identify in the longest duration, high-strain experiments. Under these conditions, grain boundary migration recrystallization was extensive, enhancing equilibration of the quartz Ti content, and thereby eliminating the driving force for diffusion. The observed Ti flux into quartz grains is consistent with the fact that quartz was undersaturated in Ti during experiments. These observations lead us to interpret the preserved CL resorption halos as patterns of incomplete Ti diffusion that developed as rutile dissolved Ti into quartz (Fig. 5).

Halos in CL intensity were measured from 315 quartz-rutile pairs from four experimental samples: a 39 h hydrostatic experiment and 39, 63, and 87 h deformation experiments (Table 1, Fig. 5). The average mid-concentration distance of the measured diffusion profiles increases with increasing experiment duration but is indistinguishable for samples from low-strain and annealing experiments that were run for the same duration (Table 1).

When applied to natural samples, geospeedometry requires independent temperature constraints to calculate the amount of time required to form the measured profile. In experiments, temperature is controlled and experiment duration is known, allowing us to test the accuracy of the geospeedometry method and the associated assumptions. To first order, geospeedometry results accurately reflect populations of diffusive timescales for each sample that correspond with increasing experiment duration. However, using published data for Ti diffusion in quartz, the calculated timescales are longer than the known experiment duration, indicating that Ti diffusion in quartz was enhanced under the conditions of our experiments.

4.3. *Diffusion of Ti in deforming, wet quartz*

Geospeedometry results indicate that Ti diffusion in our samples was faster than predicted by the one-atmosphere diffusion experiments of Cherniak et al. (2007) (Fig. 6). Diffusivities calculated from our annealing and low-strain experiments are ~2 orders of magnitude faster than those predicted by Cherniak et al. (2007), and the calculated diffusivity in our highest strain experiment is approximately a factor of 3 greater than in the low-strain and hydrostatic experiments. Cherniak et al. (2007) measured Ti diffusion between quartz and rutile, titanite, and Ti-oxides at 1-atm, anhydrous conditions. In contrast, in our experiments diffusion occurred between quartz and rutile at high-pressure, under hydrous conditions, and within quartz that was either statically annealing or dynamically recrystallizing. Here we discuss the effects of pressure, water content, and deformation as possible explanations for the high Ti diffusivities observed in our experiments.

It is unlikely that the higher pressure of our experiments is directly responsible for the greater diffusivities. In general, the activation volume for diffusion is of minor importance for most silicates over the pressure range of the crust (e.g. Bejina et al., 2003). Furthermore, it would result in lower diffusivities at higher pressure, whereas we observe the opposite.

Instead, elevated pressures could have an indirect effect on diffusivities by increasing water fugacity. Water fugacity has potential to influence Ti diffusion by increasing the concentration of Si vacancies, enhancing Ti diffusion via vacancy mechanisms. The effect of water fugacity (or pressure under hydrous conditions) on diffusion limited processes in quartz has been well documented for Si diffusion (Farver and Yund, 2000), O diffusion (Farver and Yund, 1991), ductile rheology (Kohlstedt et al., 1995; Holyoke and Kronenberg, 2013), and dislocation recovery (Tullis and Yund, 1989). A water fugacity effect on cation diffusion has also been shown for olivine (Hier-Majumder et al., 2005; Costa and Chakraborty, 2008) and plagioclase (Yund and Snow, 1989). Our results suggest that elevated water fugacities resulted in a ~2 order of magnitude enhancement of Ti diffusivities at the P–T conditions of experiments. Equivalent diffusivities measured from both hydrostatically annealed and low-strain deformed samples suggest that elevated water fugacity is the primary cause for enhanced Ti diffusion in our experiments.

Overall, tests of deformation geospeedometry using our experimental samples are consistent with experimental conditions, but indicate some potentially-important differences from the previously determined Ti volume diffusivities. Our findings suggest that bulk Ti diffusivities may be enhanced under conditions of high water fugacity and potentially also by deformation and recrystallization processes in quartz. Applications of geospeedometry to quartz deformed in hydrous, high-pressure natural settings may require consideration of the effect of water fugacity on diffusivity.

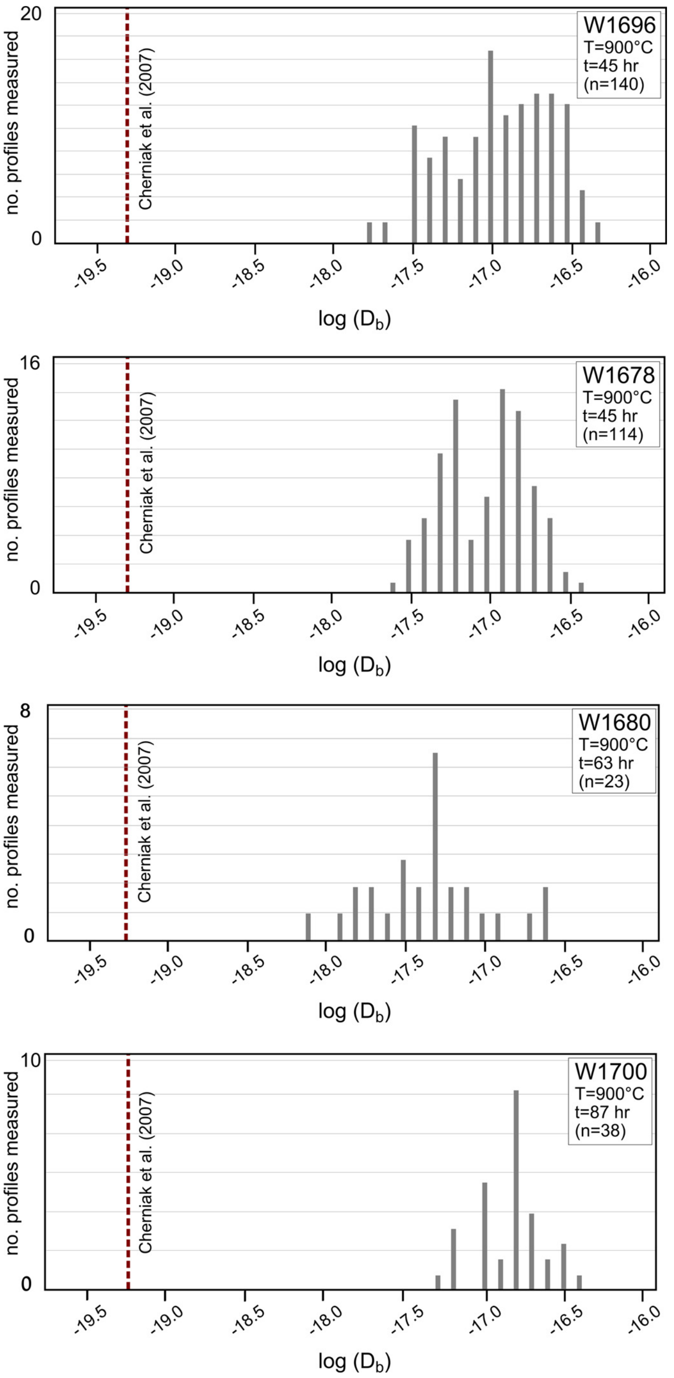

Fig. 6. Bulk diffusive mobility coefficients (D_b) solved for Ti in deforming quartz at the conditions of our experiments are approximately two orders of magnitude greater than rates of volume diffusion determined from experiments of Cherniak et al. (2007).

5. Application to naturally deformed quartz

We selected quartz mylonites from the detachment of the Pioneer Core Complex (PCC) (Idaho, USA) to test the applicability of diffusion geospeedometry for determining deformation timescales of a natural shear zone. The PCC is ideal for this purpose because its exhumation history has been evaluated by multiple geochronometers, defining a T–t path for comparison with our geospeedometry results. In addition, exhumation of the PCC was accommodated by the Wildhorse Shear Zone (WSZ), composed of a continuous section of plastically deformed quartzite mylonites in which quartz grains are densely and pervasively rutilated, allowing geospeedometry results to be compared between multiple samples across the width of the shear zone. Deformation temperatures are estimated from quartz microstructures, previously-published conventional metamorphic thermometry, and new results from Ti-in-quartz thermometry. By estimating both temperature and time from quartz using independent methods, geospeedometry results provide reliable estimates of deformation timescales and strain rates during exhumation of the PCC.

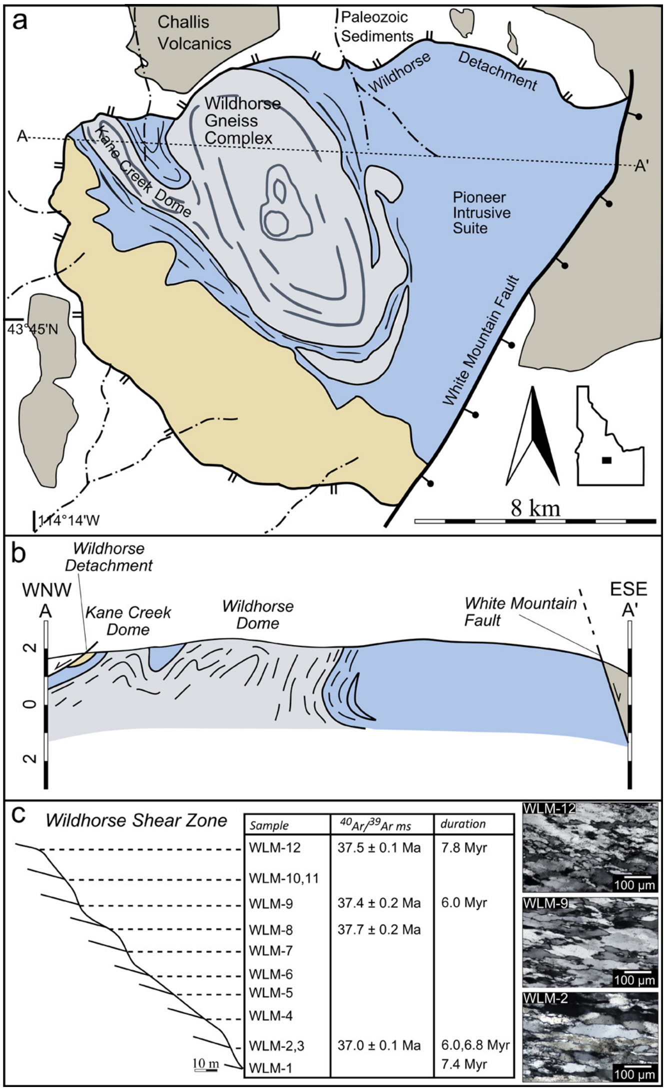

Sample	$^{40}Ar/^{39}Ar$ ms	duration
WLM-12	37.5 ± 0.1 Ma	7.8 Myr
WLM-10,11		
WLM-9	37.4 ± 0.2 Ma	6.0 Myr
WLM-8	37.7 ± 0.2 Ma	
WLM-7		
WLM-6		
WLM-5		
WLM-4		
WLM-2,3	37.0 ± 0.1 Ma	6.0,6.8 Myr
WLM-1		7.4 Myr

Fig. 7. Details of geologic field setting. (A) Simplified geologic map of the Pioneer core complex (after Wust, 1986; Vogl et al., 2012), (B) cross section showing structural relationships in the complex (after McFadden et al., 2015), and sample transect showing location, $^{40}Ar/^{39}Ar$ ages (from McFadden et al., 2015), duration results from geospeedometry, and representative quartz microstructures from different levels of the Wildhorse Shear Zone.

5.1. Geologic setting and sample description

The PCC is a domal culmination of metamorphic rocks in the hinterland of the Sevier orogenic belt (Fig. 7). It has been interpreted as a Cordilleran-style metamorphic core complex that formed following gravitational collapse of the Sevier orogen (Wust, 1986; Vogl et al., 2012). The PCC preserves abundant evidence for melt-present deformation in the footwall and detachment zone, indicated by overprinting relationships and narrow age windows for cross-cutting and transposed melt injection features (Vogl et al., 2012). Post-magmatic deformation in the PCC coincides with brittle-ductile detachment faulting and infiltration of meteoric fluids (McFadden et al., 2015). The PCC is distinct from other Cordilleran core complexes in that it records a longer time interval from syn-magmatic dome deformation (50–46 Ma) to post-magmatic detachment deformation (38–33 Ma) (Vogl et al., 2012).

The PCC is comprised of a lower plate of variably- and complexly-deformed Archean gneisses and Eocene granitoids and an upper plate of unmetamorphosed Paleozoic sediments and Tertiary volcanic and sedimentary strata (Fig. 7) (Wust, 1986; Silverberg, 1990; Diedesch, 2011). The upper and lower plates are juxtaposed along the brittle-ductile Wildhorse Shear Zone (WSZ), a ∼2 km package of mylonitized, metamorphosed, and intruded metasedimentary units that accommodated much of the Cenozoic extensional strain in the PCC (Wust, 1986; Silverberg, 1990; Diedesch, 2011; Vogl et al., 2012). Within the footwall, the WSZ grades downward with progressively higher melt fraction and deformation intensity into the Pioneer Intrusive Suite and complexly deformed gneisses of the Wildhorse Gneiss Complex (Fig. 7). The upper part of the WSZ is the Wildhorse Detachment System (WDS), a W-dipping brittle extensional feature that juxtaposes unmetamorphosed hangingwall against ductiley sheared footwall of the middle plate (Wust, 1986; Diedesch, 2011). Based on coincidence between kinematic indicators on the detachment surface and underlying mylonites of the middle plate, detachment faulting is interpreted to reflect a direct progression from higher-temperature ductile shearing to lower temperature brittle faulting during extension-related exhumation.

The WSZ is comprised of Neoproterozoic–Ordovician quartzite, marble, calc-silicate, and metapelite estimated to be c. 1.8–2.1 km in vertical thickness (Diedesch, 2011). Near the top of the WSZ (∼250 m below the detachment), deformation was partially localized within a continuous sequence (∼100–150 m) of quartz mylonites composed of the Kinnikinic Formation. The Kinnikinic quartzite is an Ordovician quartz arenite that contains detrital zircons of Meso- and Paleoproterozoic and Archean ages (Diedesch, 2011). Quartz in the Kinnikinic is targeted for geospeedometry analysis because recrystallized quartz grains contain abundant microscopic rutile needles that are strongly aligned into the lineation direction (Fig. 2A–D).

Microstructures of deformed quartz from the Kinnikinic Formation are used as additional independent information on the conditions of deformation. Quartz microstructures suggest dynamic recrystallization was accommodated via combined grain-boundary bulging and progressive subgrain rotation recrystallization overprinting a coarser grain fabric (Fig. 7C, Fig. S1) (Hirth and Tullis, 1992; Hirth et al., 2001; Law, 2014). At the top of the Kinnikinic section, quartz microstructures are characterized by elongate quartz ribbons, the long axis of which is sub-parallel to the foliation plane, that are mantled by subgrains defining an oblique fabric. In the middle of the section, subgrains are present but less abundant, and small grain boundary bulges are found along the margins of quartz ribbons that commonly display undulose extinction with a weak checkered pattern. At the base of the section, quartz grains are slightly flattened and elongated into the shear plane and exhibit sweeping undulose extinction. Subgrains are poorly developed at the base of the section, but grain boundary bulges are nearly ubiquitous along quartz boundaries. Overall these quartz microstructures suggest modest deformation temperatures of approximately 375–450 °C (Hirth et al., 2001; Law, 2014).

5.2. Existing time–temperature data

The age of exhumation of the PCC has been determined for the high-grade core and in the detachment zone. High-grade metamorphism and melt-present deformation occurred in the lower plate and at the base of the middle plate in the Eocene (Vogl et al., 2012). U–Pb ages of monazite and zircon from layered migmatites, magmatically-foliated granodiorites, and folded and boudinaged leucogranitic intrusions range from 50–46 Ma (Vogl et al., 2012). A high-angle cross-cutting leucocratic dike was dated at 46 Ma, interpreted to reflect the cessation of syn-magmatic deformation in the high grade core. The timing of deformation in the detachment zone is evaluated by: (a) ^{40}Ar/^{39}Ar ages of mica grains, which indicate cooling below ~400 °C by 38–35 Ma (Silverberg, 1990; McFadden et al., 2015) and (b) ^{40}Ar/^{39}Ar ages of K-feldspar, which indicate cooling below ~200 °C by 33 Ma (Silverberg, 1990). These geochronological data define a gap in ages spanning ~8 Myr between the early, syn-magmatic deformation of the footwall and lower-temperature detachment deformation.

Deformation temperatures in the WSZ are derived from metapelitic units located near the base of the middle plate. The highest temperatures recorded in the middle plate are found in contact aureoles 25 m from intrusions of the PIS, where assemblages indicate temperatures above the second sillimanite isograd, suggesting $T > 650\,^{\circ}\mathrm{C}$ at moderate pressures (Pattison and Tracy, 1991). At 400 m from the contact with the PIS, assemblages are characterized by cordierite-andalusite-staurolite (garnet absent) in gneissic quartzite, indicating temperatures of 500–700 °C and 0.2–0.6 GPa (Silverberg, 1990). Calculations from garnet-biotite and garnet-plagioclase thermometry in schists near the base of the middle plate indicate temperatures in the range of 590–690 °C (Silverberg, 1990).

5.3. Ti-in-quartz thermometry

Titanium contents of quartz in the Kinnikinic quartz mylonite are used to estimate deformation temperatures using the Ti-in-quartz (TitaniQ) thermobarometer (Wark and Watson, 2006; Thomas et al., 2010). Obtaining accurate measurements of Ti concentrations from rutilated quartz was challenging because of the high density of rutile needles (Fig. S1). To avoid contaminated analyses, we take our lowest-Ti population of SIMS measurements as representative. Titanium concentrations in quartz are 16–19 ppm from the top of the section (WLM-12), 3–6 ppm in quartz grains from mylonites from the middle of the section (WLM-9), and 0.5 ppm in cross-cutting veins (Table 1). There is abundant rutile (both nodular and acicular) throughout the thin sections, supporting the assumption of $a_{\mathrm{TiO_2}} = 1$. A pressure of 0.3 GPa was assumed, based on assemblages found in contact aureoles in schist adjacent to intrusions of the PIS (Silverberg, 1990) that indicate $P = 0.3$–0.5 GPa (Pattison and Tracy, 1991) and Al-in-hornblende barometry in metapelites near the base of the middle plate that indicates $P = 0.2$–0.28 GPa (Silverberg, 1990). Given these assumptions, the measured Ti contents correspond to temperatures of 450–470 °C at the top of the section and 370–390 °C in the quartz grain interiors and 280 °C in the cross-cutting vein quartz in the middle of the section. We interpret Ti-in-quartz temperature results to reflect ductile deformation within the WSZ over the range of 370–470 °C. Low Ti-in-quartz temperatures in cross-cutting veins suggest an onset of brittle deformation at approximately 300 °C. It is important to note that our assumptions of $a_{\mathrm{TiO_2}}$ and pressure correspond to minimum temperature estimates; assuming lower $a_{\mathrm{TiO_2}}$ or higher pressure will only act to increase Ti-in-quartz temperatures.

5.4. Diffusion geospeedometry applied to the Wildhorse Shear Zone

Rutile needles were exsolving from quartz during extensional deformation and exhumation of the WSZ. Burial and residence of the Kinnikinic quartzite in the middle crust during the Eocene would have homogenized quartz with a uniformly high Ti content (e.g., 70 ppm Ti for 650 °C and 7 kbar). Dynamic recrystallization of quartz during exhumation of the WSZ re-equilibrated Ti contents to the conditions of deformation and was synchronous with exsolution of rutile, as indicated by symmetrical CL halos extending in all directions from lineated and boudinaged rutile needles (Fig. 3A, B). Deformation geospeedometry was tested to reconstruct the history of the WSZ by modeling diffusion profiles from five samples across the 100 m shear zone. Two samples from the same outcrop location (WLM-2 and WLM-3) were analyzed separately to evaluate reproducibility. Measurements of profile widths and geospeedometry results are shown in Fig. 8 and Table 1.

As a first approximation we fit the diffusion profiles assuming a temperature of 500 °C, reflecting the upper range of temperatures from Ti-in-quartz thermometry and lower range of temperatures from conventional thermometry. At this temperature the diffusion profiles indicate deformation timescales of ~5–10 Myr. By linking constraints from field geology and geochronology with results of geospeedometry and microstructure analysis, we can evaluate the appropriateness of assumptions behind the geospeedometry method and better understand the deformation conditions of the WSZ.

Results from high and low-temperature geochronology reveal a hiatus in deformation ages over an ~8 Myr window between the cessation of melt-present deformation (46 Ma; Vogl et al., 2012) and the earliest closure ages of ^{40}Ar/^{39}Ar in muscovite (38 Ma; Silverberg, 1990; McFadden et al., 2015) (Fig. 9). This age window is consistent with other lines of structural and field evidence for deformation in the PCC. Structural offset of the Summit Creek stock and the North Fork Lake quartz porphyry dike complex indicates displacements of 15–16 and 30–32 km, respectively (Wust, 1986; Silverberg, 1990; Vogl et al., 2012). Applying our geospeedometry results to this structural offset indicates strain rates of $\sim 1 \times 10^{-12}\ \mathrm{s}^{-1}$ if we assume deformation localized within the 100 m quartzite unit or $\sim 6 \times 10^{-14}\ \mathrm{s}^{-1}$ if we assume deformation was distributed across the 2 km detachment zone. Geospeedometry results are also consistent with typical displacement rates for major crustal normal faults of ~3–5 $\mathrm{mm\,yr^{-1}}$ (Hacker et al., 1990; Phillips et al., 2004), equating to displacement timescales of ~4–7 Myr with modest assumptions for structural offset (20 km).

However, while the timescale estimates from geospeedometry appear to be consistent with independent constraints, there are multiple lines of evidence to suggest that deformation persisted to temperatures significantly below 500 °C (the value assumed for modeling diffusion profiles), and this must be reconciled if we are to be confident in the results of our geospeedometry analysis. First, the ^{40}Ar/^{39}Ar ages of muscovite indicate recrystallization continued to temperatures of ~400 °C at 38 Ma (McFadden et al., 2015). Second, the quartz microstructures indicate BLG and SGR recrystallization overprinting an earlier GBM grain fabric with approximate average diameters of 10 μm (Fig. 7C, S1), corresponding to stresses of ~100 MPa (Stipp and Tullis, 2003); at 100 MPa and 400 °C, quartzite flow laws predict strain rates of $2 \times 10^{-12}\ \mathrm{s}^{-1}$ (Hirth et al., 2001). In contrast, strain rates of $\sim 5 \times 10^{-11}\ \mathrm{s}^{-1}$ at 500 °C are faster than predications from the integration of the geologic or thermochronologic data, even assuming minimum fault offsets. Third, it is likely that most of our SIMS measurements sampled regions of quartz that correspond to the high-CL "background" as appears in Fig. 3A, B and Fig. 8; in this case the equilibrium Ti concentration at the time of exsolution (directly adjacent to the exsolving needle; see Fig. 4) would be considerably less than es-

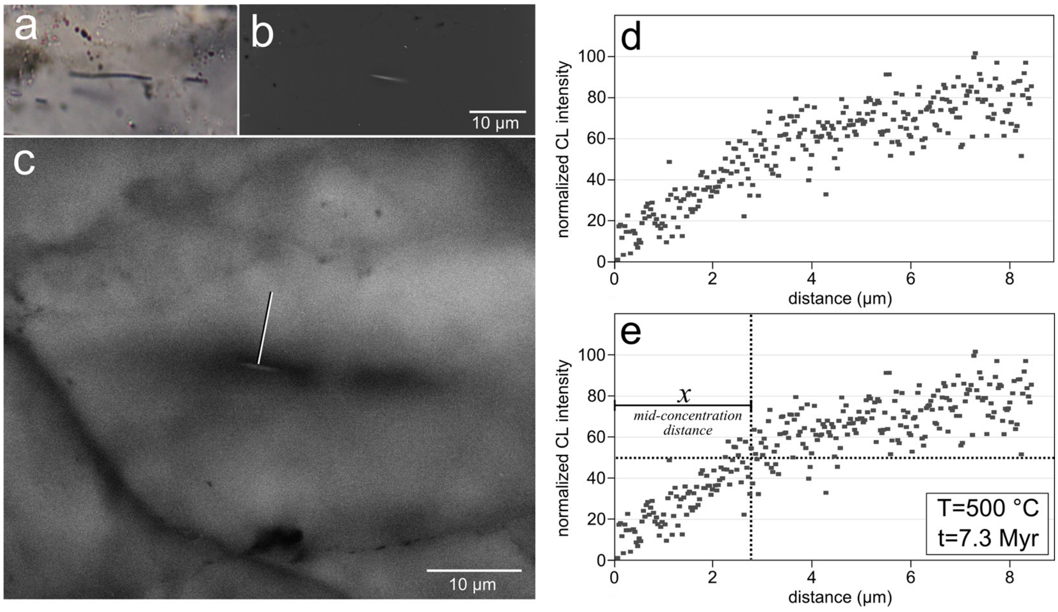

Fig. 8. Technique for modeling Ti diffusion profiles around rutile needles as applied to depletion halos present in natural samples. The intersection of a rutile needle with the thin section surface is identified in petrographic microscope (A), detected in a secondary electron image (B), and analyzed with cathodoluminescence (C) to measure the surrounding Ti concentration field. A dark CL halo (C) suggests that Ti was diffusing from quartz into rutile. The gradient in CL intensity is measured along a linear transect from rutile into the surrounding quartz (C), revealing a composition profile in inferred Ti content that resembles a diffusion profile (D). Profiles are normalized to a concentration percent of 0–100, trimmed from max–min, and the mid-concentration distance is calculated. By assuming a fixed temperature, geospeedometry results indicate durations of 5–10 Myr for samples from the Pioneer Core Complex (E).

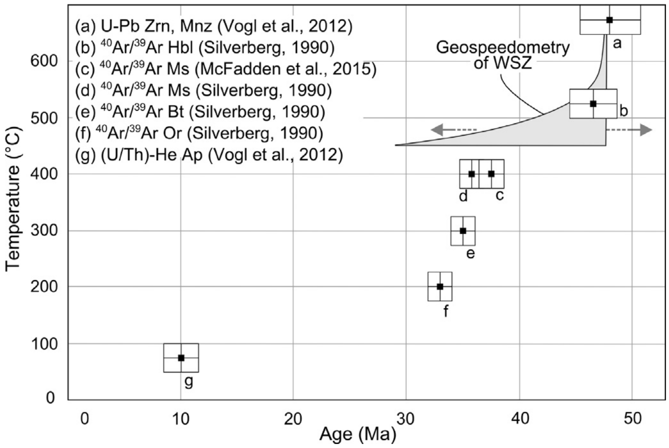

Fig. 9. Temperature–time history of deformation in the Wildhorse Shear Zone. Results from deformation geospeedometry form a wedge-shaped region that can be translated in absolute time. Results from geospeedometry are consistent with the deformation history as defined by ages from multiple geochronometers.

timated by our Ti-in-quartz thermometry. Finally, the summary of the thermochronology data shown in Fig. 9 indicates that it is unrealistic to assume that deformation was sustained at 500 °C (with no cooling) for the time indicated by geospeedometry results.

Taken together, these observations suggest that either (a) deformation persisted to considerably lower temperatures than indicated by results of diffusion modeling (requiring an enhanced diffusivity to explain the development of profiles at lower T) or (b) the profiles formed at higher T and were undisturbed during deformation at lower T. If quartz continued to deform to temperatures of ~400 °C, one would expect diffusion profiles to also reflect this deformation, but there is no evidence for this in our observed symmetrical CL halos (Fig. 3A, B). This leads us to speculate that diffusivities may have been enhanced by hydrous conditions prevailing during deformation, as suggested by our experiments (Fig. 6).

To extrapolate our lab-derived bulk diffusivities to the conditions of natural samples, we scale the experimental results using the differences in water fugacity. Water fugacities are calculated using the Pitzer and Sterner (1994) equation of state for pure water to be 1.8 GPa for experiments and ~100 MPa at the estimated P–T conditions of natural samples (Table 1). Given that T–t conditions of our experiments are known, we can use geospeedometry results to derive an "enhanced" Ti mobility for wet quartz at the experimental fugacity and extrapolate this to the conditions of natural samples. For our 900 °C experiments, we measure a bulk Ti diffusivity of $\sim 1 \times 10^{-17}$ $\mathrm{m^2\,s^{-1}}$ (Table 1, Fig. 6). We do not have constraints on the activation energy for Ti diffusion in quartz at hydrous conditions, so we conservatively use the value for dry Ti diffusion (273 $\mathrm{kJ\,mol^{-1}}$) derived by Cherniak et al. (2007). One might expect a similar activation energy for hydrous conditions, as changes in vacancy concentration resulting from elevated water fugacity would have a greater influence on the effective pre-exponential constant than the activation energy (as is the case for hydrous diffusion in olivine; see Kohlstedt, 2006). We calculate a pre-exponential constant for the conditions of our experiments and normalize this to the conditions of natural samples assuming linear dependence on water fugacity, as observed for creep. At 470 °C this enhanced Ti diffusivity is 4×10^{-26} $\mathrm{m^2\,s^{-1}}$, which equates to deformation timescales of 4 Myr and strain rates of 2×10^{-12} $\mathrm{s^{-1}}$, in agreement with constraints from structural offset, geochronology ages, and typical fault displacement rates. Taking this one step further, if a 400 °C deformation temperature is assumed (corresponding to quartz microstructures and recrystallized grain sizes), it requires an activation energy ~25 $\mathrm{kJ\,mol^{-1}}$ lower than reported by Cherniak et al. (2007) to produce strain rates that agree with independent constraints. This analysis suggests that the effect of water fugacity on enhancement of Ti diffusivities could have modest but potentially important outcomes when extrapolated to natural settings.

6. Conclusions

We modeled incomplete diffusion profiles around kinematically oriented inclusions in two suites of deformed samples to test the applicability of diffusion geospeedometry for reconstructing timescales and strain rates of ductile deformation. Rutile needle inclusions in mylonitized quartz grains provide an ideal situation to test shear zone geospeedometry because they behave as diffusion couples and are sensitive to deformation kinematics. Given the wide range of conditions under which quartz deforms plastically, it is likely that quartz was recrystallizing over a prolonged interval of an orogenic event. By modeling diffusion progress between rutile needles and the host quartz, we solve for the duration over which needles were aligned in their kinematic framework. Assuming that high aspect ratio inclusions rotate into the lineation direction after small strains, these timescales represent a minimum duration that a deformation event was sustained. Quantifying shear zone deformation directly from the strain-accommodating mineral itself (quartz) is a new approach that provides independent estimates on the history of ductility in shear zones.

We have tested geospeedometry of rutilated quartz mylonites on samples from the Pioneer Core Complex, where results indicate deformation of the quartzite shear zone lasted for approximately 5–10 Myr, consistent with an 8 Myr period of shear zone deformation as defined by existing geochronology (Vogl et al., 2012) and with results of geodynamic models simulating core complex exhumation in the North American Cordillera (Stevens et al., 2017). Using geospeedometry results paired with estimates of structural offset accommodated by the Wildhorse Shear Zone, we calculate paleo strain rates of 10^{-12} s^{-1} that are similar to past estimates from other continental shear zones (Pfiffner and Ramsay, 1982; Hacker et al., 1990; Hirth et al., 2001; Sassier et al., 2009).

Testing shear zone geospeedometry on experimental samples where the T–t conditions are known yields trends that are relatively accurate but reveals discrepancies between bulk diffusion coefficients determined from our high-pressure deformation experiments and volume diffusion coefficients determined from previous one-atmosphere calibration experiments (Cherniak et al., 2007). These differences likely reflect the importance of water fugacity, and perhaps also deformation and recrystallization processes, on diffusive mobility of Ti in quartz. Our results are consistent with accelerated diffusion and mineral reaction in phases that are deforming via dislocation-related mechanisms and further motivate additional experimental and theoretical research to better understand effects of deformation and recrystallization processes on mineral compositions.

Acknowledgements

This research was supported by a collaborative NSF grant awarded to DW–CT (EAR-0911497) and GH (EAR-0911536). WN would like acknowledge a GSA Graduate Student Research Grant, a UMN Thesis Research Travel Grant, and two short courses that motivated aspects of this research: the MSA *Diffusion in Minerals in Melts* short course and the joint MSA/DMG *Diffusion Modeling Workshop* at Ruhr University. The authors thank H. Lowers for assistance with EPMA and SEM-CL analysis at USGS–Denver and N. Shimizu and B. Monteleone for assistance with SIMS analysis at WHOI. Y. Zhang and an anonymous reviewer provided detailed reviews that improved the quality of this manuscript.

Appendix A. Supplementary material

Supplementary material related to this article can be found online at https://doi.org/10.1016/j.epsl.2018.06.025.

References

Béjina, F., Jaoul, O., Liebermann, R.C., 2003. Diffusion in minerals at high pressure: a review. Phys. Earth Planet. Inter. 139 (1–2), 3–20. https://doi.org/10.1016/S0031-9201(03)00140-7.

Bouchez, J.L., Mainprice, D.H., Trepied, L., Doukhan, J.C., 1984. Secondary lineation in a high-T quartzite (Galicia, Spain): an explanation for an abnormal fabric. J. Struct. Geol. 6 (1–2), 159–165. https://doi.org/10.1016/0191-8141(84)90093-2.

Camacho, A., Yang, P., Frederiksen, A., 2009. Constraints from diffusion profiles on the duration of high-strain deformation in thickened crust. Geology 37 (8), 755–758. https://doi.org/10.1130/G25753A.1.

Chakraborty, S., 2008. Diffusion in solid silicates: a tool to track timescales of processes comes of age. Annu. Rev. Earth Planet. Sci. 36 (1), 153–190. https://doi.org/10.1146/annurev.earth.36.031207.124125.

Cherniak, D.J., Watson, E.B., Wark, D.A., 2007. Ti diffusion in quartz. Chem. Geol. 236 (1–2), 65–74. https://doi.org/10.1016/j.chemgeo.2006.09.001.

Clay, P.L., Baxter, E.F., Cherniak, D.J., Kelley, S.P., Thomas, J.B., Watson, E.B., 2010. Two diffusion pathways in quartz: a combined UV-laser and RBS study. Geochim. Cosmochim. Acta 74 (20), 5906–5925. https://doi.org/10.1016/j.gca.2010.07.014.

Costa, F., Chakraborty, S., 2008. The effect of water on Si and O diffusion rates in olivine and implications for transport properties and processes in the upper mantle. Phys. Earth Planet. Inter. 166 (1–2), 11–29. https://doi.org/10.1016/j.pepi.2007.10.006.

Diedesch, T., 2011. Kinematic Analysis of the Wildhorse Detachment Fault. Idaho State University.

Dunlap, W.J., Teyssier, C., McDougall, I., Baldwin, S., 1991. Ages of deformation from K/Ar and ^{40}Ar/^{39}Ar dating of white micas. Geology 19 (12), 1213–1216. https://doi.org/10.1130/0091-7613(1991)019<1213:AODFKA>2.3.CO.

Farver, J.R., Yund, R.A., 1991. Measurement of oxygen grain boundary diffusion in natural, fine-grained, quartz aggregates. Geochim. Cosmochim. Acta 55, 1597–1607.

Farver, J., Yund, R., 2000. Silicon diffusion in a natural quartz aggregate: constraints on solution-transfer diffusion creep. Tectonophysics 325 (3–4), 193–205. https://doi.org/10.1016/S0040-1951(00)00121-9.

Freeman, S.R., Butler, R.W.H., Cliff, R.A., Rex, D.C., 1998. Direct dating of mylonite evolution: a multi-disciplinary geochronological study from the Moine Thrust Zone, NW Scotland. J. Geol. Soc. 155 (5), 745–758. https://doi.org/10.1144/gsjgs.155.5.0745.

Hacker, B.R., Yin, A., Christie, J.M., Snoke, A.W., 1990. Differential stress, strain rate, and temperatures of mylonitization in the Ruby Mountains, Nevada: implications for the rate and duration of uplift. J. Geophys. Res. 95 (89), 8569–8580.

Hier-Majumder, S., Anderson, I.M., Kohlstedt, D.L., 2005. Influence of protons on Fe–Mg interdiffusion in olivine. J. Geophys. Res., Solid Earth 110 (2). https://doi.org/10.1029/2004JB003292.

Hirth, G., Teyssier, C., Dunlap, J., 2001. An evaluation of quartzite flow laws based on comparisons between experimentally and naturally deformed rocks. Int. J. Earth Sci. 90 (1), 77–87. https://doi.org/10.1007/s005310000152.

Hirth, G., Tullis, J., 1992. Dislocation creep regimes in quartz aggregates. J. Struct. Geol. 14 (2), 145–159.

Holyoke, C.W., Kronenberg, A.K., 2013. Reversible water weakening of quartz. Earth Planet. Sci. Lett. 374, 185–190. https://doi.org/10.1016/j.epsl.2013.05.039.

Kohlstedt, D.L., 2006. The role of water in high-temperature rock deformation. Rev. Mineral. Geochem. 62 (1), 377–396.

Kohlstedt, D.L., Evans, B., Mackwell, S.J., 1995. Strength of the lithosphere: constraints imposed by laboratory experiments. J. Geophys. Res. 100 (B9), 17587–17602.

Law, R.D., 2014. Deformation thermometry based on quartz c-axis fabrics and recrystallization microstructures: a review. J. Struct. Geol. 66, 129–161. https://doi.org/10.1016/j.jsg.2014.05.023.

Leeman, W.P., MacRae, C.M., Wilson, N.C., Torpy, A., Lee, C.-T., Student, J.J., Thomas, J.B., Vicenzi, E.P., 2012. A study of cathodoluminescence and trace element compositional zoning in natural quartz from volcanic rocks: mapping titanium content in quartz. Microsc. Microanal. 18, 1322–1341. https://doi.org/10.1017/S1431927612013426.

McFadden, R.R., Mulch, A., Teyssier, C., Heizler, M., 2015. Eocene extension and meteoric fluid flow in the Wildhorse detachment, Pioneer metamorphic core complex, Idaho. Lithosphere 4, 355–367. https://doi.org/10.1130/L429.1.

Mitra, S., 1976. A quantitative study of deformation mechanisms and finite strain in quartzites. Contrib. Mineral. Petrol. 59, 203–226.

Mulch, A., Cosca, M.A., 2004. Recrystallization or cooling ages: in situ UV-laser ^{40}Ar/^{39}Ar geochronology of muscovite in mylonitic rocks. J. Geol. Soc. 161 (4), 573–582. https://doi.org/10.1144/0016-764903-110.

Müller, A., Wiedenbeck, M., van den Kerkhof, A.M., Kronz, A., Simon, K., 2003. Trace elements in quartz – a combined electron microprobe, secondary ion mass spectrometry, laser-ablation ICP-MS, and cathodoluminescence study. Eur. J. Mineral. 15 (4), 747–763. https://doi.org/10.1127/0935-1221/2003/0015-0747.

Müller, W., Aerden, D., Halliday, A.N., 2000. Isotopic dating of strain fringe increments: duration and rates of deformation in Shear Zones. Science 288 (5474), 2195–2198. https://doi.org/10.1126/science.288.5474.2195.

Nachlas, W.O., Hirth, G., 2015. Experimental constraints on the role of dynamic recrystallization on resetting the Ti-in-quartz thermobarometer. J. Geophys. Res., Solid Earth 120, 8120–8137. https://doi.org/10.1002/2015JB012274.

Nachlas, W.O., Whitney, D.L., Teyssier, C., Bagley, B., Mulch, A., 2014. Titanium concentration as a record of multiple deformation mechanisms in an extensional shear zone. Geochem. Geophys. Geosyst. 15 (4), 1374–1397. https://doi.org/10.1002/2013GC005200.

Olker, B., Altherr, R., Paquin, J., 2003. Fast exhumation of the ultrahigh-pressure Alpe Arami garnet peridotite (Central Alps, Switzerland): constraints from geospeedometry and thermal modelling. J. Metamorph. Geol. 21 (4), 395–402.

Pattison, D.R.M., Tracy, R.J., 1991. Phase equilibria and thermobarometry of metapelites. Rev. Mineral. Geochem. 26 (1), 105–206.

Pfiffner, O., Ramsay, J., 1982. Constraints on geological strain rates: arguments from finite strain states of naturally deformed rocks. J. Geophys. Res. 87 (B1), 311–321.

Phillips, R.J., Parrish, R.R., Searle, M.P., 2004. Age constraints on ductile deformation and long-term slip rates along the Karakoram fault zone, Ladakh. Earth Planet. Sci. Lett. 226 (3–4), 305–319. https://doi.org/10.1016/j.epsl.2004.07.037.

Pitzer, K.S., Sterner, S.M., 1994. Equations of state valid continuously from zero to extreme pressures for H_2O and CO_2. J. Chem. Phys. 101 (4), 3111–3116. https://doi.org/10.1063/1.467624.

Sassier, C., Leloup, P.H., Rubatto, D., Galland, O., Yue, Y., Lin, D., 2009. Direct measurement of strain rates in ductile shear zones: a new method based on syntectonic dikes. J. Geophys. Res. 114 (B1). https://doi.org/10.1029/2008JB005597.

Schneider, S., Hammerschmidt, K., Rosenberg, C.L., 2013. Dating the longevity of ductile shear zones: insight from ^{40}Ar/^{39}Ar in situ analyses. Earth Planet. Sci. Lett. 369–370, 43–58. https://doi.org/10.1016/j.epsl.2013.03.002.

Sherlock, S.C., Kelley, S.P., Zalasiewicz, J.A., Schofield, D.I., Evans, J.A., Merriman, R.J., Kemp, S.J., 2003. Precise dating of low-temperature deformation: strain-fringe analysis by ^{40}Ar–^{39}Ar laser microprobe. Geology 31 (3), 219–222. https://doi.org/10.1130/0091-7613(2003)031<0219:PDOLTD>2.0.CO;2.

Silverberg, D.S., 1990. The Tectonic Evolution of the Pioneer Metamorphic Core Complex, South-Central Idaho. Massachusetts Institute of Technology.

Stevens, L.M., Bendick, R., Baldwin, J.A., 2017. Synconvergent exhumation of metamorphic core complexes in the northern North American Cordillera. Geology 45 (6), G38802.1. https://doi.org/10.1130/G38802.1.

Stipp, M., Tullis, J., 2003. The recrystallized grain size piezometer for quartz. Geophys. Res. Lett. 30 (21), 2088. https://doi.org/10.1029/2003GL018444.

Thomas, J.B., Bruce Watson, E., Spear, F.S., Shemella, P.T., Nayak, S.K., Lanzirotti, A., 2010. TitaniQ under pressure: the effect of pressure and temperature on the solubility of Ti in quartz. Contrib. Mineral. Petrol. 160 (5), 743–759. https://doi.org/10.1007/s00410-010-0505-3.

Tullis, J., Yund, R.A., 1989. Hydrolytic weakening of quartz aggregates: the effects of water and pressure on recovery. Geophys. Res. Lett. 16 (11), 1343–1346.

Vogl, J.J., Foster, D.A., Fanning, C.M., Kent, K.A., Rodgers, D.W., Diedesch, T., 2012. Timing of extension in the Pioneer metamorphic core complex with implications for the spatial-temporal pattern of Cenozoic extension and exhumation in the northern US, Cordillera. Tectonics 31. https://doi.org/10.1029/2011TC002981.

Wark, D.A., Watson, E.B., 2006. TitaniQ: a titanium-in-quartz geothermometer. Contrib. Mineral. Petrol. 152 (6), 743–754. https://doi.org/10.1007/s00410-006-0132-1.

Watson, E.B., Baxter, E.F., 2007. Diffusion in solid-Earth systems. Earth Planet. Sci. Lett. 253 (3–4), 307–327. https://doi.org/10.1016/j.epsl.2006.11.015.

Williams, M.L., Jercinovic, M.J., 2002. Microprobe monazite geochronology: putting absolute time into microstructural analysis. J. Struct. Geol. 24, 1013–1028.

Wust, S.L., 1986. Extensional deformation with northwest vergence, Pioneer core complex, central Idaho. Geology 14 (8), 712–714. https://doi.org/10.1130/0091-7613(1986)14<712:EDWNVP>2.0.CO;2.

Yund, R.A., Snow, E., 1989. Effects of hydrogen fugacity and confining pressure on the interdiffusion rate of NaSi–CaAl in Plagioclaste. J. Geophys. Res. 94 (B8), 10662–10668.

Zhang, X.Y., Watson, E.B., Cherniak, D.J., 2007. Oxygen self-diffusion “fast-paths” in titanite single crystals and a general method for deconvolving self-diffusion profiles with “tails”. Geochim. Cosmochim. Acta 71 (6), 1563–1573. https://doi.org/10.1016/j.gca.2006.12.013.

Zhang, Y., Cherniak, D., 2010. Diffusion in minerals and melts. Rev. Mineral. Geochem. 72, 1038.